arXiv:2505.15906v2 [cond-mat.supr-con] 22 Feb 2026

Pairing mechanism and superconductivity in pressurized $La_5Ni_3O_{11}$

Ming Zhang,[1,*] Cui-Qun Chen,[2,*] Dao-Xin Yao,[2,†] and Fan Yang[3,‡]

[1] *Zhejiang Key Laboratory of Quantum State Control and Optical Field Manipulation, Department of Physics, Zhejiang Sci-Tech University, 310018 Hangzhou, China*

[2] *Center for Neutron Science and Technology, Guangdong Provincial Key Laboratory of Magnetoelectric Physics and Devices, State Key Laboratory of Optoelectronic Materials and Technologies, School of Physics, Sun Yat-Sen University, Guangzhou 510275, China*

[3] *School of Physics, Beijing Institute of Technology, Beijing 100081, China*

The discovery of superconductivity (SC) with critical temperature T_c above the boiling point of liquid nitrogen in pressurized $La_3Ni_2O_7$ has sparked a surge of exploration of high-T_c superconductors in the Ruddlesden-Popper (RP) phase nickelates. More recently, the RP phase nickelate $La_5Ni_3O_{11}$, which hosts a layered structure with alternating bilayer and single-layer NiO_2 planes, has been reported to accommodate SC under pressure, exhibiting a dome-shaped pressure dependence with highest $T_c \approx 64$ K, capturing a lot of interest. Here, using density functional theory (DFT) and random phase approximation (RPA) calculations, we systematically study the electronic properties and superconducting mechanism of this material. Our DFT calculations yield a band structure including two nearly decoupled sets of sub-band structures, with one set originating from the bilayer subsystem and the other from the single-layer one. RPA-based analysis demonstrates that SC in this material occurs primarily within the bilayer subsystem exhibiting an $s^{\pm}$ wave pairing symmetry similar to that observed in pressurized $La_3Ni_2O_7$, while the single-layer subsystem mainly serves as a bridge facilitating the inter-bilayer phase coherence through the interlayer Josephson coupling (IJC). Since the IJC thus attained is extremely weak, it experiences a prominent enhancement under pressure, leading to the increase of the bulk T_c with pressure initially. When the pressure is high enough, the T_c gradually decreases due to the reduced density of states on the γ-pocket. In this way, the dome-shaped pressure dependence of T_c observed experimentally is naturally understood.

The discovery of superconductivity (SC) with critical temperature $T_c \approx 80$ K in the Ruddlesden-Popper (RP) phase bilayer nickelate $La_3Ni_2O_7$ under pressure [1] has sparked significant experimental and theoretical interest in the field [2–45]. Subsequently, researchers observed SC in the trilayer nickelate $La_4Ni_3O_{10}$ under pressure, and recently detected SC in ambient-pressure (AP) $La_3Ni_2O_7$ thin films [46–49]. These findings further underscore the potential of RP-phase nickelates as high-T_c superconductors [50–57]. In RP phase nickelates with the general formula $R_{n+1}Ni_nO_{3n+1}$ (R = rare earth), each Ni forms a NiO_6 octahedron with corner-sharing O atoms. At AP, bilayer $La_3Ni_2O_7$ and trilayer $La_4Ni_3O_{10}$ manifest octahedral tilting and in-plane lattice anisotropy [1, 46, 55]. Upon increasing pressure, both the octahedral tilting and the in-plane lattice constant disparity gradually diminish and eventually the crystal structures attain higher symmetry ($I4/mmm$ space group) [58].

Furthermore, hybrid RP phase nickelates, formed by alternating stacking different RP phases along the c-axis, also attract widespread investigations, especially the hybridization of the single-layer La_2NiO_4, the bilayer $La_3Ni_2O_7$ and the trilayer $La_4Ni_3O_{10}$ [59–63]. Until now, successful synthesis of 1313 phase ($La_3Ni_2O_7$) [60, 61] and 1212 phase ($La_5Ni_3O_{11}$) [62] has been achieved. A previous study reported a superconducting transition onset temperature up to 80 K in alternating stacking single-layer La_2NiO_4 and trilayer $La_4Ni_3O_{10}$, namely 1313 phase [61]. However, it remains unclear whether the observed high-T_c comes from the hybrid 1313 phase or 2222 bilayer phase.

Recently, pressure-induced SC with maximal $T_c = 64$ K was observed in the hybrid 1212 phase, i.e. $La_5Ni_3O_{11}$ [64]. Transport and magnetic torque measurements also revealed a density-wave (DW) transition at ambient and low pressures. In contrast to the previously reported DW in $La_3Ni_2O_7$ and $La_4Ni_3O_{10}$, the DW observed here is notably robust against pressure. Intriguingly, SC emerges at around 11.7 GPa and exhibits a dome-shaped pressure-dependent behavior, in contrast to the previously reported right-triangle-like behavior observed in pressurized $La_3Ni_2O_7$ [58]. Previous random-phase approximation (RPA) based study proposed that d-wave is the leading pairing symmetry that originates from the La_2NiO_4 single-layer in the material [65]. However, recent studies using combined density functional theory (DFT) and dynamic-mean-field-theory (DMFT) provide another possibility that the La_2NiO_4 single-layer in $La_5Ni_3O_{11}$ is nearly Mott-insulating which does not carry SC [63, 66], consistent with previous insight that the pure La_2NiO_4 is an antiferromagnetic (AFM) Mott insulator [67, 68]. Therefore, a more systematic investigation into the electronic and superconducting properties of the hybrid 1212 phase $La_5Ni_3O_{11}$ is urgently needed.

In this paper, we adopt the first-principle DFT calculations to study the electronic structure of $La_5Ni_3O_{11}$, followed by a RPA based study to clarify the superconduct-

* These two authors contributed equally to this work.
† yaodaox@mail.sysu.edu.cn
‡ yangfan_blg@bit.edu.cn

ing mechanism in this material. Based on our DFT band structure, we construct a trilayer $(d_{z^2}, d_{x^2-y^2})$-orbital tight-binding (TB) model, in which the hopping integrals between the bilayer subsystem and the single-layer one is very weak, reflecting that the two subsystems are almost decoupled, allowing for the two parts to be treated separately. Our RPA based analysis suggests that the superconducting pairing mainly occurs in the bilayer subsystem, which takes the $s^{\pm}$-pattern similar with that in pressurized $La_3Ni_2O_7$, while the single-layer subsystem mainly serves as a bridge connecting adjacent superconducting bilayer subsystems to establish phase coherence along the c-axis necessary for the bulk SC, through the interlayer Josephson coupling (IJC). As the IJC is extremely weak, it will experience prominent enhancement with the increase of the pressure, leading to enhancement of the T_c in the low pressure regime. When the pressure is strong enough, the T_c decreases with further enhancement of the pressure due to a reduction in the density of states (DOS) on the γ-pocket crucial for pairing. Therefore, our study provides a natural understanding of the dome-shaped pressure dependence of the T_c observed in the experiment. Furthermore, our findings elucidate the distinct pressure responses of hybrid-phase and pure-phase nickelate superconductors, offering a unified framework that may also be extended to other hybrid superconducting systems.

Results

Band Structure and TB model

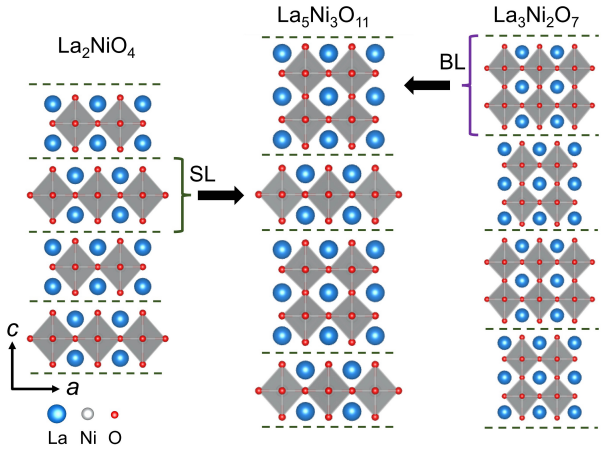


FIG. 1. (color online) Side view of crystal structures of the single-layer (La_2NiO_4), bilayer ($La_3Ni_2O_7$) and SL-BL ($La_5Ni_3O_{11}$) RP phase nickelates. The blue, grey, and red balls represent lanthanum, nickel, and oxygen atoms, respectively.

$La_5Ni_3O_{11}$ is a single-layer-bilayer (SL-BL) stacked nickelate, as shown in Fig. 1. La_2NiO_4 and $La_3Ni_2O_7$ stack alternatively in the RP phase, crystallizing into an orthorhombic phase ($Cmmm$ or $Immm$ space group) at AP and transitioning to $P4/mmm$ space group under high pressure (HP) [62, 64]. DFT calculated phonon spectra show imaginary frequencies at AP whereas the imaginary frequencies vanish under HP for $P4/mmm$ phase (see Fig.S1 [69]), demonstrating a structural phase transition under pressure and the structural stability of $P4/mmm$ phase under high pressure. Unlike bulk $La_3Ni_2O_7$, the out-of-plane Ni-O-Ni angle in $La_5Ni_3O_{11}$ remains 180° from AP to HP, without octahedral rotation. Therefore, in $La_5Ni_3O_{11}$ each unit cell contains only one Ni atom per layer, in contrast to the cases of bulk $La_3Ni_2O_7$ and $La_4Ni_3O_{10}$ in which each unit cell contains two Ni atoms per layer at AP due to octahedral rotation.

The band structure of the SL-BL stacking $La_5Ni_3O_{11}$ at 12 GPa is shown in Fig. 2(a), consistent with previous theoretical results [63, 66]. As in most RP phase nickelates, bands around the Fermi level can be described by the Ni-e_g sector. The SL-derived Ni-d_{z^2} band lies between the BL-derived bonding and anti-bonding bands. Compared to the band structure at AP (see Fig.S2 [69]), the BL-derived bonding band is metalized by pressure, leaving the γ pocket at the brillouin zone (BZ) corner, as shown in Fig. 2(b). This phenomenon resembles the behavior of pressurized bulk $La_3Ni_2O_7$.

To further investigate the electronic properties in $La_5Ni_3O_{11}$, we perform Wannier downfolding on the Ni-d_{z^2} and $d_{x^2-y^2}$ orbitals based on the DFT electronic structure. The obtained TB Hamiltonian in real space can be expressed as

$$H_{\mathrm{TB}} = \sum_{\boldsymbol{r}_i \Delta \boldsymbol{r} \mu\nu\sigma} t_{\Delta \boldsymbol{r}\mu\nu} c^{\dagger}_{\boldsymbol{r}_i\mu\sigma} c_{(\boldsymbol{r}_i+\Delta\boldsymbol{r})\nu\sigma}. \quad (1)$$

Here $\boldsymbol{r}_i$ represents the coordinates of site i, $\Delta \boldsymbol{r}_x(\Delta \boldsymbol{r}_y) \in (-2, 2)$ represents the hoppings up to the third-nearest neighbor. In this context, $\boldsymbol{r}_i$ refers to the unit cell index, while a finite $\Delta \boldsymbol{r}$ represents the interunit cell separation. The indices $\mu, \nu = 1, \cdots, 6$ containing the d_{z^2} and $d_{x^2-y^2}$ orbitals of the upper and lower layers of the bilayer subsystem, as well as those of the single-layer subsystem. The SL-BL lattice and corresponding hoppings are depicted in Fig. 2(c), with the hopping integrals $t_{ij}^{\mu\nu}$ provided in Tab. I. Note that due to the RP stacking in $La_5Ni_3O_{11}$, a $(\frac{1}{2}, \frac{1}{2})$ translation exists between the bilayer and single-layer sublattice. Fig. 2(d) displays the band structure for TB model, which is in good agreement with DFT results. The obtained FS for this TB model contains five pockets labeled as α, α', β, γ, γ', as shown in Fig. 2(b). The dominant component orbital of γ and γ' pockets is d_{z^2}, while the α, α' and β pockets are the mix of d_{z^2} and $d_{x^2-y^2}$ orbitals. From the right half of Fig. 2(b), we can see that the α' and γ' pocket are contributed from single-layer subsystem while the other three pockets from bilayer subsystem.

As shown in Tab. I, the coupling between the single-layer subsystem and the bilayer subsystem is extremely weak, with the strongest hopping integral amplitude between the two parts being $\left|t^{z,BS}_{[\frac{1}{2},\frac{1}{2}]}\right|$=0.0103 eV. The sole effect

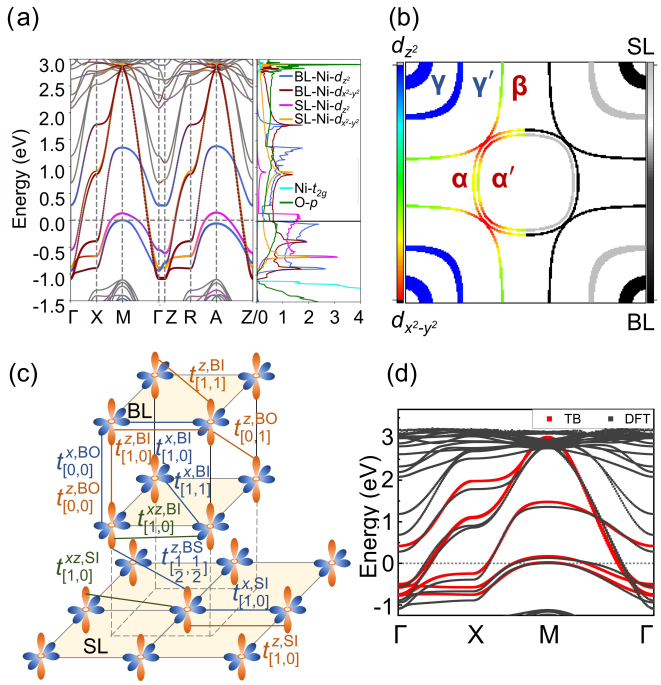


FIG. 2. (color online) Band structure of the DFT and six-orbital TB model for $La_5Ni_3O_{11}$ at 12 GPa. (a) DFT band structure and projected DOS of $La_5Ni_3O_{11}$. (b) FS in the BZ, with the five pockets labeled. The color scheme in the left half of (b) represents the relative contributions of the d_{z^2} and $d_{x^2-y^2}$ orbital, while the colors scheme on the right half of (b) indicates the relative contributions from Ni atoms in the single-layer and bilayer subsystems. (c) Schematic of $La_5Ni_3O_{11}$ lattice of six-orbital TB model. The dashed line denotes the $(\frac{1}{2},\frac{1}{2})$ translation of RP stacking between bilayer and single-layer sublattice. (d) The TB band structure corresponding to (c).

of such a weak coupling is to equilibrate the chemical potentials of the two subsystems and thereby adjust the electron filling. Consequently, it is reasonable to treat the two subsystems separately.

The decoupling of the two subsystems at the TB Hamiltonian level is achieved by modifying the summation over μ and ν in Eq. 1. Specifically, restricting $\mu,\nu \in (1,\cdots,4)$ and electron filling $n \approx 3.1$ which got from SL-BL system yields the Hamiltonian of the bilayer subsystem, while restricting $\mu,\nu \in (5,6)$ and electron filling $n \approx 1.9$ yields that of the single-layer subsystem. A comparison between the band structure of the bilayer subsystem and that of $La_5Ni_3O_{11}$ (SL-BL system) is shown in Fig. 3(a), where it can be seen that the bilayer subsystem reproduces the key features of the bilayer-derived bands in the full system. The three FS pockets of the bilayer subsystem, labeled α, β, and γ, are shown in Fig. 3(b), and are clearly separated from the five pockets observed in Fig. 2(b). Fig. 3(c) shows that the band structure of the single-layer subsystem matches well with the single-layer-derived bands of the full SL-BL system. The two Fermi pockets of the single-layer subsystem, corresponding to the α' and γ' pockets of the full system, are shown in Fig. 3(d).

The separation of the single-layer and bilayer subsystems within the TB framework points toward an underlying layer-selective character in this hybrid RP-phase

TABLE I. Hopping parameters and site energies of TB model for $La_5Ni_3O_{11}$ at 12 GPa in unit of eV. Here, x, z and xz denotes hopping within and between $d_{x^2-y^2}$, d_{z^2} orbitals, respectively. The abbreviations BI, BO, and SI represent intra-bilayer, inter-bilayer, and single-layer in-plane hoppings, respectively, while BS denotes hoppings between bilayer and single-layer units. The TB model includes hopping processes up to the third-nearest neighbor, i.e., [2,0]. ϵ denotes the on-site energy.

$t^{z,BI}_{[1,0]}$	$t^{z,BI}_{[1,1]}$	$t^{xz,BI}_{[1,0]}$	$t^{x,BI}_{[1,0]}$	$t^{x,BI}_{[1,1]}$	$t^{z,BO}_{[0,0]}$	$t^{z,BO}_{[1,0]}$
-0.1125	-0.0180	0.2373	-0.4708	0.0661	-0.6713	0.0202
$t^{z,BO}_{[1,1]}$	$t^{x,BO}_{[0,0]}$	$t^{x,BO}_{[1,0]}$	$t^{x,BO}_{[1,1]}$	$t^{xz,BO}_{[1,0]}$	$t^{z,BS}_{[\frac{1}{2},\frac{1}{2}]}$	$t^{z,SI}_{[1,0]}$
0.0065	0.0132	-0.0013	0.0017	-0.0320	-0.0103	-0.0886
$t^{z,SI}_{[1,1]}$	$t^{xz,SI}_{[1,0]}$	$t^{x,SI}_{[1,0]}$	$t^{x,SI}_{[1,1]}$	$t^{z,BI}_{[2,0]}$	$t^{xz,BI}_{[2,0]}$	$t^{x,BI}_{[2,0]}$
-0.0108	0.1901	-0.4522	0.0752	-0.0192	0.0344	-0.0686
$t^{z,SI}_{[2,0]}$	$t^{xz,SI}_{[2,0]}$	$t^{x,SI}_{[2,0]}$	ϵ^B_z	ϵ^B_x	ϵ^S_z	ϵ^S_x
-0.0121	0.0256	-0.0590	0.3288	0.8648	0.1360	0.9313

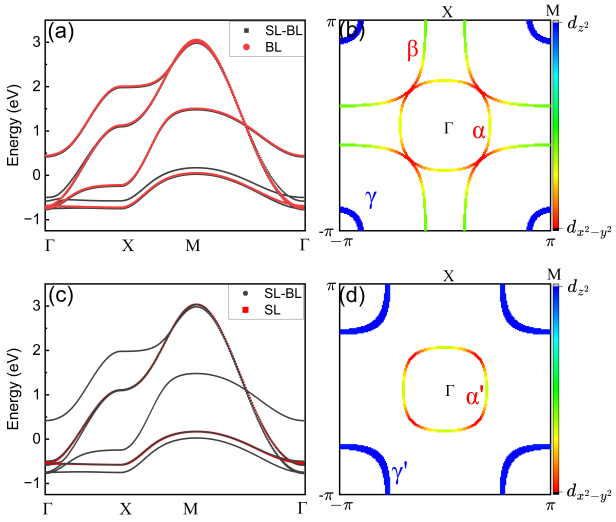


FIG. 3. (color online) TB bands and FS characteristics of the BL and SL subsystems in $La_5Ni_3O_{11}$ (SL-BL system) at 12 GPa. (a) Band structure of the SL-BL system (black lines) and that of the isolated BL subsystem (red lines). (b) FS of the isolated BL subsystem, showing that the α pocket is primarily composed of $d_{x^2-y^2}$ orbitals, the β pocket contains contributions from both $d_{x^2-y^2}$ and d_{z^2} orbitals, and the γ pocket originates mainly from d_{z^2} orbitals. (c) Band structure of the SL-BL system (black lines) and the isolated SL subsystem (red lines). (d) FS of the isolated SL subsystem, showing that the α' pocket is primarily composed of $d_{x^2-y^2}$ orbitals, the γ' pocket originates mainly from d_{z^2} orbitals.

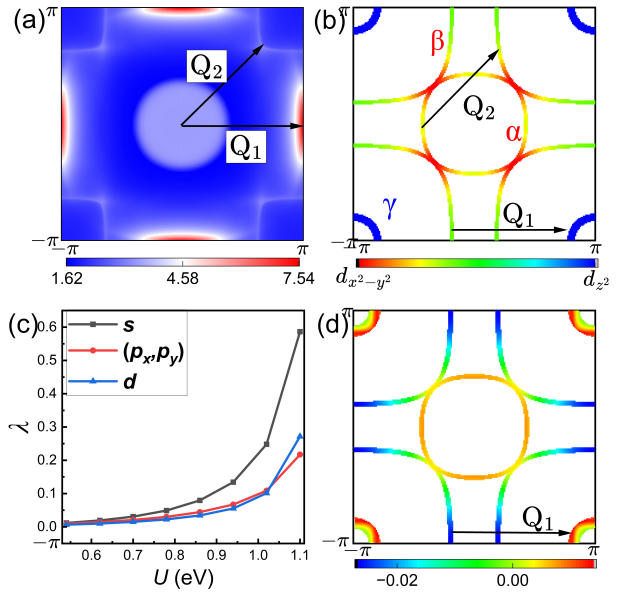


FIG. 4. (color online) (a) Distribution of the largest eigenvalue of the spin susceptibility matrix $\chi^s(q)$ in the BZ in the bilayer subsystem for $U = 1$ eV and $J_H = U/6$. The susceptibility peaks at two inequivalent momenta, denoted as Q_1 and Q_2, respectively. (b) FS of the bilayer subsystem in the BZ at 12 GPa. As shown in (b), Q_1 corresponds to a nesting vector between the β and γ pockets, while Q_2 corresponds to a nesting vector between the α and β pockets. (c) The largest pairing eigenvalue λ of the various pairing symmetries as function of the interaction strength U with fixed $J_H = U/6$. (d) The distributions of the leading s-wave pairing gap function on the FS for $U = 1.1$ eV, exhibiting an $s^{\pm}$-pattern.

nickelate. At ambient and low pressures, the incorporation of local dynamical correlations via the DMFT modifies the DFT band structure by removing the FS pockets contributed by the single-layer subsystem, leaving only the three FS pockets contributed by the bilayer subsystem [63, 66]. This observation indicates that the single-layer subsystem is close to a Mott-insulating state, with possible AFM order present [63], analogous to the bulk La_2NiO_4 [67, 68]. At HP, the Mott gap becomes narrower, permitting a small density of mobile carriers that may suppress the AFM order [63]. Indeed, the long-range magnetic order has not been observed experimentally under HP so far [62]. Regardless of whether residual magnetic order persists or not, the single-layer subsystem remains a "bad metal" and can hardly carry SC [63]. This suggests that superconductivity is more likely to originate from the bilayer subsystem. Since DFT+DMFT indicates that electronic correlation in the bilayer subsystem is comparatively weaker, we will focus our subsequent RPA analysis on the bilayer subsystem to study its pairing instability.

RPA study of the SC

Given that superconductivity is likely to arise predominantly from the bilayer subsystem, we adopt the following multi-orbital Hubbard interaction to investigate the SC driven by electron interactions in this bilayer subsystem,

$$H_{int} = U\sum_{i\tilde{\mu}} n_{i\tilde{\mu}\uparrow}n_{i\tilde{\mu}\downarrow} + V\sum_{i,\sigma,\sigma'} n_{i1\sigma}n_{i2\sigma'} + J_H\sum_{i\sigma\sigma'}\Big[c^\dagger_{i1\sigma}c^\dagger_{i2\sigma'}c_{i1\sigma'}c_{i2\sigma} + (c^\dagger_{i1\uparrow}c^\dagger_{i1\downarrow}c_{i2\downarrow}c_{i2\uparrow} + h.c.)\Big]. \quad (2)$$

Here, U, V, and J_H denote the intra-orbital, inter-orbital Hubbard repulsion, and the coupling of Hund (and the pair hopping) respectively, which satisfy the relation $U = V + 2J_H$. $\tilde{\mu} \in (1, 2)$ labels the two orbitals (d_{z^2} and $d_{x^2-y^2}$) associated with each Ni atom. i denotes the lattice sites belonging to the bilayer subsystem. We employ the multi-orbital RPA approach [70–76] to treat this Hamiltonian. By renormalization, the spin susceptibility $\boldsymbol{\chi}^{(s)}$ and charge susceptibility $\boldsymbol{\chi}^{(c)}$ can be defined as Eq. (3):

$$\boldsymbol{\chi}^{(s)}(\boldsymbol{k}, i\nu) = [I - \boldsymbol{\chi}^{(0)}(\boldsymbol{k}, i\nu)U^{(s)}]^{-1}\boldsymbol{\chi}^{(0)}(\boldsymbol{k}, i\nu),$$
$$\boldsymbol{\chi}^{(c)}(\boldsymbol{k}, i\nu) = [I + \boldsymbol{\chi}^{(0)}(\boldsymbol{k}, i\nu)U^{(c)}]^{-1}\boldsymbol{\chi}^{(0)}(\boldsymbol{k}, i\nu). \quad (3)$$

Where $\boldsymbol{\chi}^{(0)}$ is bare susceptibility for the non-interacting case, expressed as a tensor $\boldsymbol{\chi}^{(0)pq}_{st}$, with p, q, s, t as orbital indices. Similarly, $\boldsymbol{\chi}^{(s)}$ can be expressed as $\boldsymbol{\chi}^{(s)pq}_{st}$. $U^{(s,c)}$ is the renormalized interaction strength, which is represented as a $4^2 \times 4^2$ matrix in the bilayer subsystem. Note that there is a critical interaction strength $U_c^{(s/c)}$ for the spin/charge susceptibility. When $U \geq U_c^{(s,c)}$, the denominator matrix in Eq. (3) will have zero eigenvalues for certain values of $\boldsymbol{k}$, causing the renormalized spin or charge susceptibility to diverge. This divergence indicates the onset of magnetic or charge order. Generally, repulsive Hubbard interactions suppress the charge susceptibility, but enhance the spin susceptibility [70–76]. Therefore, $U_c^{(s)} < U_c^{(c)}$ and we denote $U_c^{(s)}$ as U_c in the bilayer subsystem in the following. When fixing $J_H = U/6$, we find $U_c \approx 1.15$ eV.

Defining $\chi^s(\boldsymbol{q})$ as the maximum eigenvalue of $\boldsymbol{\chi}^{(s)}$ at the momentum $\boldsymbol{q}$, Fig. 4(a) shows its distribution in the BZ for $U = 1$ eV$< U_c$ of the bilayer subsystem. Notably, the distribution exhibits peaks at two unequivalent momenta, which we have labeled as $\mathbf{Q}_1$ and $\mathbf{Q}_2$. These two momenta precisely correspond to the two FS nesting vectors of the bilayer subsystem, as illustrated in Fig. 4(b), and the vector $\mathbf{Q}_1 = (\pi, 0)$ is associated with the highest intensity of spin susceptibility, which is very similar to the case of bulk $La_3Ni_2O_7$ under pressure [16, 18].

When $U < U_c$, the spin fluctuations can mediate SC in the bilayer subsystem, whose T_c is related to the largest pairing eigenvalue λ via $T_c \propto \omega_D e^{-1/\lambda}$ [73], where the "Debye frequency" ω_D represents the typical energy scale of spin fluctuations. The pairing symmetry is determined by the corresponding eigenvector (see **Methods**). Fig. 4(c) illustrates the dependence of the largest pairing

eigenvalue, denoted as λ, on the interaction strength U for different potential pairing symmetries. The D_{4h} point group of this bilayer subsystem structure allows for several possible pairing symmetries. In Fig. 4(c), we show the three leading pairing symmetries: s-wave, d-wave, and degenerate (p_x, p_y)-wave pairings. It is clear that the s-wave is the leading pairing symmetry and dominates other ones. The gap function of the obtained s-wave pairing is shown on the FS in Fig. 4(d), which displays the $s^{\pm}$ pattern. Consequently, the α- and γ- pockets connected by the nesting vector $\mathbf{Q}_1$ are distributed with the strongest pairing amplitude, with opposite gap signs. This pairing pattern is also similar to that in pressurized bulk $La_3Ni_2O_7$ [6, 16, 18].

Pressure Dependence of the SC

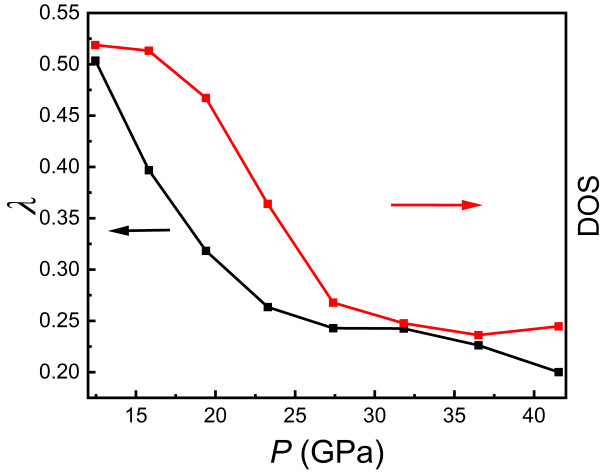


FIG. 5. (color online) Pressure-dependence of the pairing eigen value λ (black solid line) and the DOS on the γ-pocket (red solid line).

To investigate the pressure dependence of SC in the system, we first performed DFT calculations of the electronic band structure under pressures ranging from approximately 12 to 40 GPa. The corresponding key hopping parameters at each pressure are listed in Tab. II. Based on these TB results, we employed the RPA approach to calculate the pairing eigenvalue λ as a function of pressure P. As shown in Fig. 5, the resulting λ exhibits a downward trend with enhanced P, which originates from reduced DOS on the γ pocket.

The decreasing $\lambda \sim P$ relation caused by the reduced DOS shown in Fig. 5 parallels that in the bulk $La_3Ni_2O_7$ [3, 23, 44], which closely matches the experimentally observed $T_c \sim P$ relation in that material [58]. However, it seems at a glance that such a decreasing $\lambda \sim P$ relation conflicts with the $T_c \sim P$ relation in $La_5Ni_3O_{11}$, which shows a pronounced increase up to around 20 GPa, followed by a gradual decline afterward [64]. The discrepancy between the $\lambda \sim P$ and the $T_c \sim P$ relations in $La_5Ni_3O_{11}$ originates from that its alternating SL-BL structure brings into extremely weak IJC, which is crucial for establishing bulk superconductivity. Since superconducting pairing originates from the bilayer subsystem while global phase coherence relies on interlayer coupling, the enhancement of IJC under pressure becomes decisive, thereby resolving the seeming contradiction. In the following, we clarify this viewpoint.

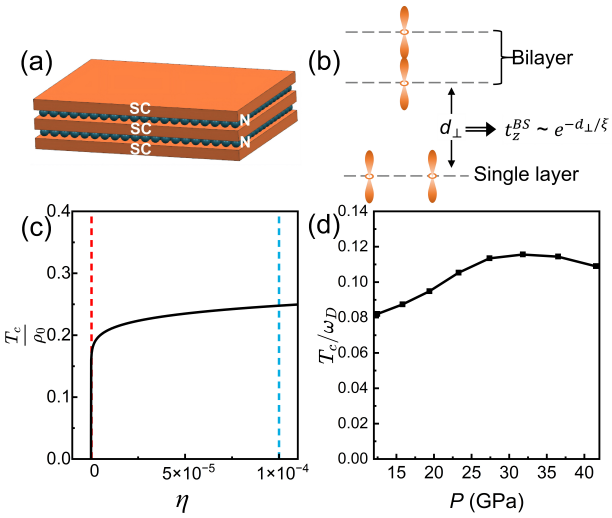


FIG. 6. (color online) Influence of the IJC on the pressure-dependence of the T_c. (a) Schematic of the intrinsic S–N–S Josephson Junction structure of $La_5Ni_3O_{11}$, where the superconducting (S) layers correspond to the BL subsystem and the normal (N) layers correspond to the SL subsystem. (b) Schematic of the interlayer distance $d_\perp$ dependence of the hopping integral t_z^{BS} between the BL and the SL subsystems. (c) T_c/ρ_0 as a function of the anisotropy parameter η that reflects the strength of the IJC. The red dashed line marks the $\eta \approx 10^{-8}$ associated with the $La_5Ni_3O_{11}$, while the blue dashed line marks the $\eta \approx 10^{-4}$ associated with the bulk $La_3Ni_2O_7$. (d) Pressure-dependence of the superconducting T_c (in unit of ω_D) in $La_5Ni_3O_{11}$.

As shown in Fig. 6(a), the $La_5Ni_3O_{11}$ hosts alternating bilayer and single-layer NiO_2 subsystems, where the former supports SC and the latter is a "bad metal". This results in an intrinsic superconductor–normal metal–superconductor (S–N–S) Josephson Junction structure. In this structure, the establishment of bulk SC requires not only intra-bilayer pairing but also inter-bilayer phase coherence. Given that the intermediate single-layer subsystem is close to a Mott-insulating state, it may be approximated as an intermediate layer without itinerant electrons participating in superconductivity. Physically, the inter-bilayer phase coherence is established via combined tunneling of a Cooper pair from a superconducting bilayer to its adjacent one, i.e. the IJC, across the intervening normal-metallic single-layer. This is a second-order process with respect to the tiny inter-bilayer single-particle tunneling, and hence a fourth-order process with respect to the weak bilayer-single-layer tunneling for a single particle. As such attained IJC is extremely weak, it will experience a prominent enhancement with the increase of the pressure. In the following,

TABLE II. Hopping parameters and site energies of TB model for $La_5Ni_3O_{11}$ under various pressures. x, z and xz denotes hopping within and between $d_{x^2-y^2}$, d_{z^2} orbitals, respectively. The abbreviations BI, BO, and SI represent intrabilayer, interbilayer, and single-layer in-plane hoppings, respectively. Only hopping integrals greater than 1 meV are listed here for clarity. All parameters are in unit of eV.

Pressure (GPa)	ε_z^B	ε_x^B	ε_z^S	ε_x^S	$t_{[0,0]}^{z,BO}$	$t_{[1,0]}^{x,BI}$	$t_{[1,0]}^{z,BI}$	$t_{[1,0]}^{xz,BI}$	$t_{[1,0]}^{x,SI}$	$t_{[1,0]}^{xz,SI}$
12	0.334	0.915	-0.162	1.022	-0.673	-0.477	-0.113	0.241	-0.460	0.187
16	0.335	0.921	-0.163	1.024	-0.695	-0.487	-0.122	0.245	-0.469	0.192
19	0.337	0.922	-0.185	1.027	-0.724	-0.501	-0.122	0.251	-0.478	0.196
23	0.337	0.930	-0.188	1.029	-0.749	-0.511	-0.128	0.256	-0.489	0.1200
27	0.338	0.931	-0.207	1.029	-0.759	-0.523	-0.131	0.261	-0.500	0.203
32	0.338	0.941	-0.210	1.032	-0.782	-0.534	-0.136	0.266	-0.510	0.208
37	0.339	0.942	-0.221	1.036	-0.801	-0.546	-0.142	0.271	-0.523	0.212
42	0.340	0.951	-0.234	1.035	-0.812	-0.557	-0.146	0.275	-0.534	0.216

we provide a more quantitative clarification for this point.

In principle, the hopping integral t_z^{BS} between the bilayer and the single-layer subsystems can be obtained through fitting the TB model to the DFT band structure. However, due to the limited accuracy achieved in the fitting, the obtained tiny t_z^{BS} bears a considerably large relative error bar, and the accurate pressure dependence of t_z^{BS} can be hardly acquired. To overcome this difficulty, we adopt the following semi-phenomenological analysis for the problem. As shown in Fig. 6(b), the t_z^{BS} depends on the overlap between the d_{z^2} orbital wavefunctions of the bilayer and the single-layer subsystems, which decays exponentially with the displayed interlayer distance $d_\perp$, i.e. $t_z^{BS} \sim e^{-d_\perp/\xi}$, where ξ characterizes the decaying length. Consequently, the effective hopping integral between adjacent superconducting bilayers follows $t_z^{BB} \sim (t_z^{BS})^2$, and the IJC follows $J_\perp^{BB} \propto (t_z^{BB})^2 \sim (t_z^{BS})^4 \sim e^{-4d_\perp/\xi}$.

In quasi-2D layered superconductors such as $La_5Ni_3O_{11}$ and $La_3Ni_2O_7$, the bulk T_c is related to the IJC through the following relation in the limit of vanishingly weak IJC ($\eta \to 0$) [77],

$$T_c \approx \rho_0 \frac{\pi}{\ln(32/\eta)}. \tag{4}$$

Here ρ_0 indicates the intralayer phase stiffness reflecting the pairing within the bilayer subsystem, which is approximated as the pairing temperature obtained from the RPA calculation, i.e. $\omega_D e^{-1/\lambda}$. The anisotropy parameter η reflects the strength of the tiny IJC, i.e. $\eta \sim J_\perp^{BB}$. Since $J_\perp^{BB} \propto (t_z^{BS})^4$, and $t_z^{BS} \sim 10^{-2}$, we have $\eta \sim 10^{-8}$ for $La_5Ni_3O_{11}$, which is extremely weak. In contrast, for $La_3Ni_2O_7$, since there exists no intervening normal-metallic single-layer to go across, we have $\eta \sim 10^{-4}$. Substituting this into Eq. (4) yields an estimated T_c for $La_5Ni_3O_{11}$. As shown in Fig. 6(c), for $La_5Ni_3O_{11}$, the anisotropy parameter η locates within the regime where a slight enhancement of η will prominently enhance the T_c; while for $La_3Ni_2O_7$, η has only a minor effect on T_c. It should be noted that the T_c here refers to the three-dimensional bulk superconducting T_c, which exhibits true zero resistance, unlike the two-dimensional Kosterlitz–Thouless transition temperature T_{KT}, where the resistance (or conductance) exhibits a power-law decay to zero with voltage.

Under applied pressure, the strain is proportional to the pressure, implying that $\Delta d_\perp \propto -P$, i.e., $d_\perp(P) = d_\perp^0 - \kappa P$, where $d_\perp^0$ is the interlayer distance at zero pressure and κ is the modulus constant. Therefore,

$$\eta \sim e^{-4(d_\perp^0 - \kappa P)/\xi} \equiv \eta_0 e^{\alpha P}. \tag{5}$$

Here, η_0 is the anisotropy parameter at AP. Ultimately,

$$T_c \approx T_c^{\mathrm{RPA}} \frac{\pi}{\ln(\frac{32}{\eta})} \approx \omega_D e^{-1/\lambda} \frac{\pi}{\ln(\frac{32}{\eta_0 e^{\alpha P}})}. \tag{6}$$

Since t_z^{BS} is too small for DFT to capture its pressure dependence with sufficient accuracy, a precise calculation is challenging; therefore, we extract the parameters by fitting to experiment. For a reasonable set of parameters, e.g. $\eta_0 \approx 10^{-8}$ and $\alpha \approx 0.3$ GPa^{-1}, the resulting pressure dependence of T_c shown in Fig. 6(d) indeed exhibits a dome-shaped behavior similar to that observed in experiment [64].

Discussion

In this work, we investigate the electronic structure and superconducting mechanism of the hybrid RP nickelate $La_5Ni_3O_{11}$, composed of alternating single-layer and bilayer subsystems. Based on DFT and RPA calculations, we find that SC predominantly emerges in the bilayer subsystem with an $s^\pm$-wave pairing symmetry, closely resembling that in pressurized bulk $La_3Ni_2O_7$. We further show that the pressure dependence of the superconducting T_c in $La_5Ni_3O_{11}$ is governed not only by the intralayer pairing but also by the IJC, which leads to a dome-like $T_c(P)$ behavior consistent with experimental observations. Although our analysis reproduces this dome-like trend, this model should be regarded as one possible

channel to account for the observed T_c of $La_5Ni_3O_{11}$, while other channels may also be relevant.

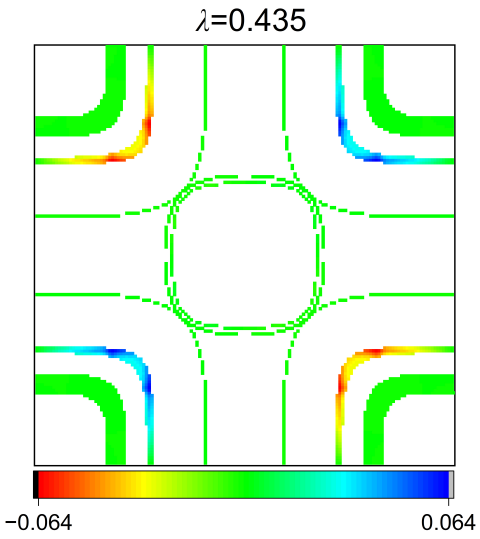


FIG. 7. (color online) The distributions of the leading d_{xy}-wave pairing gap function with $\lambda = 0.435$ at $U = 0.5$ eV, $J_H = 1/6U$.

Recently, a full monolayer–bilayer RPA study was reported in Ref. [65]. We therefore also performed a full monolayer–bilayer calculation, as shown in Fig. 7.

Methods

DFT method

DFT calculations were performed by Vienna ab initio simulation package (VASP) [78, 79], in which the projector augmented wave (PAW) [80, 81] method with a 600 eV plane-wave cutoff is applied. The generalized gradient approximation (GGA) of Perdew-Burke-Ernzerhof (PBE) form exchange correlation potential is adopted [82]. The convergence criterion of force was set to be 0.001 eV/Å and total energy convergence criterion was set to be 10^{-7} eV. A Γ-centered $19 \times 19 \times 5$ Monkhorst Pack k-mesh grid is used for primitive cell of $P4/mmm$ phase and a Γ-centered $14 \times 14 \times 5$ Monkhorst Pack k-mesh grid for primitive cell of $Cmmm$ phase. In structural relaxations, the lattice constants of $P4/mmmm$ phase we use are $a = 3.77$ Å and $c = 16.20$ Å. DFT calculations reveal that the corresponding pressure is 12 GPa, where $La_5Ni_3O_{11}$ enters superconducting state [64]. An effective Hubbard U parameter $U = 3.5$ eV was employed to account for the correlation effects of 3d electrons in Ni atoms [37, 83]. To obtain the projected TB models, we further performed Wannier downfolding as implemented in WANNIER90 [84] package, in which the good convergences were reached.

RPA method

In the standard multi-orbital RPA approach, the bare susceptibility is defined as

$$\chi_{st}^{(0)pq}(\boldsymbol{k},\tau) \equiv \frac{1}{N}\sum_{\boldsymbol{k}_1\boldsymbol{k}_2} \left\langle T_\tau c_p^\dagger(\boldsymbol{k}_1,\tau) c_q(\boldsymbol{k}_1+\boldsymbol{k},\tau) \times c_s^\dagger(\boldsymbol{k}_2+\boldsymbol{k},0) c_t(\boldsymbol{k}_2,0)\right\rangle_0, \quad (7)$$

where $\langle\cdots\rangle_0$ represents the expectation value in the free-electron state, and $p/q/s/t$ are the effective orbital indices, which label combined layer, sublattice and physical orbital indices. Transforming the above defining formula to the momentum-frequency space, we obtain the explicit formula of bare susceptibility as

$$\chi_{st}^{(0)pq}(\boldsymbol{k},i\omega_n) = \frac{1}{N}\sum_{\boldsymbol{k}_1\alpha\beta} \xi_{\alpha p}^*(\boldsymbol{k}_1)\xi_{\beta q}(\boldsymbol{k}_1+\boldsymbol{k})\xi_{\beta s}^*(\boldsymbol{k}_1+\boldsymbol{k}) \xi_{\alpha t}(\boldsymbol{k}_1)\frac{f(\varepsilon_{\boldsymbol{k}_1+\boldsymbol{k}}^\beta-\mu_c)-f(\varepsilon_{\boldsymbol{k}_1}^\alpha-\mu_c)}{i\omega_n+\varepsilon_{\boldsymbol{k}_1}^\alpha-\varepsilon_{\boldsymbol{k}_1+\boldsymbol{k}}^\beta}, \quad (8)$$

where α, β represent band indices, ε and ξ are the eigenvalue, and eigen-state of the free particle Hamiltonian, μ_c is the chemical potential, and $f(\varepsilon_{\boldsymbol{k}}) = 1/(1+e^{\beta\varepsilon_{\boldsymbol{k}}})$ is the Fermi-Dirac function.

In the RPA level, the renormalized spin/charge susceptibilities for the system are

$$\chi^{(s)}(\mathbf{q},i\nu) = [I-\chi^{(0)}(\mathbf{q},i\nu)U^{(s)}]^{-1}\chi^{(0)}(\mathbf{q},i\nu),$$
$$\chi^{(c)}(\mathbf{q},i\nu) = [I+\chi^{(0)}(\mathbf{q},i\nu)U^{(c)}]^{-1}\chi^{(0)}(\mathbf{q},i\nu). \quad (9)$$

Where $\chi^{(s,c)}(\mathbf{q},i\nu)$, $\chi^{(0)}(\mathbf{q},i\nu)$, and $U^{(s,c)}$ are operated as $l^2 \times l^2$ matrices (l represents the number of orbits and the upper or lower two indices are viewed as one number) with elements of the matrix $U^{(s/c)}$ to be

$$U_{st}^{(s)pq} = \begin{cases} U, & p=q=s=t \\ J_H, & p=q\neq s=t \\ J_H, & p=s\neq q=t \\ V, & p=t\neq s=q \end{cases}$$

$$U_{st}^{(c)pq} = \begin{cases} U, & p=q=s=t \\ 2V-J_H, & p=q\neq s=t \\ J_H, & p=s\neq q=t \\ 2J_H-V, & p=t\neq s=q \end{cases}$$

Since we only consider the on-site interaction, the elements of the matrix $U^{(s/c)}$ are non-zero only if p, q, s, t are the same layer indices.

Note that there is a critical interaction strength $U_c^{(s,c)}$ for spin and charge respectively. When $U > U_c^{(s,c)}$, the denominator matrix in Eq. 9 will have zero eigenvalues for some q and the renormalized spin or charge susceptibility diverges there, which invalidates the RPA treatment [43, 70–74, 76, 85, 86]. This divergence of spin susceptibility for $U > U_c^{(s)}$ implies magnetic order, while that of the charge susceptibility for $U > U_c^{(c)}$ implies charge order.

When $U < U_c$, a Cooper pair $c_t(\mathbf{q})c_s(-\mathbf{q})$ could be scattered to $c_p^\dagger(\mathbf{k})c_q^\dagger(-\mathbf{k})$ by exchanging charge or spin fluctuations. Considering only intra-band pairings, we obtain the following effective pairing interaction:

$$V_{eff} = \frac{1}{N}\sum_{\alpha\beta\mathbf{kq}} V^{\alpha\beta}(\mathbf{k},\mathbf{q})c_\alpha^\dagger(\mathbf{k})c_\alpha^\dagger(-\mathbf{k})c_\beta(-\mathbf{q})c_\beta(\mathbf{q}) \tag{10}$$

Here α/β is band indice. And effective pairing interaction vertex $V^{\alpha\beta}(\mathbf{k},\mathbf{q})$ has the form:

$$V^{\alpha\beta}(\mathbf{k},\mathbf{q}) = \sum_{pqst}\Gamma_{pq}^{st}(\mathbf{k},\mathbf{q})\xi_p^{\alpha,*}(\mathbf{k})\xi_q^{\alpha,*}(-\mathbf{k})\xi_s^{\beta}(-\mathbf{q})\xi_t^{\beta}(\mathbf{q}). \tag{11}$$

Here $\xi^\alpha(\mathbf{k})$ are the eigenvector corresponding to α-th eigenvalue (relative to the chemical potential μ_c) of the TB Hamiltonian matrices. Within the mean-field approximation, one can derive a self-consistent equation for the pairing gap, which when linearized near T_c [43, 70–74, 76, 85, 86] yields the linearized gap equation (12):

$$\Delta_\alpha(\mathbf{k}) = -\sum_{\beta\mathbf{q}} V^{\alpha\beta}(\mathbf{k},\mathbf{q}) \times \frac{\tanh(\frac{\beta_c}{2}|\tilde{\varepsilon}_\beta(\mathbf{q})|)}{|\tilde{\varepsilon}_\beta(\mathbf{q})|} \times \Delta_\beta(\mathbf{q}). \tag{12}$$

Here $\beta_c = \frac{1}{k_B T_c}$ represents the critical temperature of SC. Choosing a thin energy shell near the Fermi level, Eq. (12) becomes the eigenvalue problem of the effective interaction matrix $V^{\alpha\beta}$, which determines the T_c and the leading pairing symmetry of the system. To be specific, $\Delta_\alpha(\mathbf{k})$ represents the relative gap function on the α-th FS patches near T_c, and eigenvalue λ is related to T_c through $\lambda^{-1} = \ln(1.13\frac{\hbar\omega_D}{k_B T_c})$. The leading pairing symmetry is determined by the largest eigenvalue λ of Eq. (13):

$$-\frac{1}{(2\pi)^2}\sum_\beta \oint_{FS} dq_\parallel \frac{V^{\alpha\beta}(\mathbf{k},\mathbf{q})}{v_F^\beta(\mathbf{q})}\Delta_\beta(\mathbf{q}) = \lambda\Delta_\alpha(\mathbf{k}). \tag{13}$$

Data availability

Relevant data supporting the key findings of this study are available within the article and the Supplementary Information file. All raw data generated during the current study are available from the corresponding authors upon reasonable request.

Code availability

The code that supports the plots within this paper is available from the corresponding author upon reasonable request.

References

[1] Sun, H. *et al.* Signatures of superconductivity near 80 K in a nickelate under high pressure. *Nature* **621**, 493–498 (2023). URL https://doi.org/10.1038/s41586-023-06408-7.

[2] Luo, Z., Hu, X., Wang, M., Wú, W. & Yao, D.-X. Bilayer two-orbital model of $La_3Ni_2O_7$ under pressure. *Physical Review Letters* **131**, 126001 (2023). URL https://doi.org/10.1103/PhysRevLett.131.126001.

[3] Huo, Z. *et al.* Modulation of the octahedral structure and potential superconductivity of $La_3Ni_2O_7$ through strain engineering. *Science China Physics, Mechanics & Astronomy* **68**, 237411 (2025). URL https://doi.org/10.1007/s11433-024-2583-y.

[4] Zhang, Y., Lin, L.-F., Moreo, A. & Dagotto, E. Electronic structure, dimer physics, orbital-selective behavior, and magnetic tendencies in the bilayer nickelate superconductor $La_3Ni_2O_7$ under pressure. *Phys. Rev. B* **108**, L180510 (2023). URL https://doi.org/10.1103/PhysRevB.108.L180510.

[5] Lechermann, F., Gondolf, J., Bötzel, S. & Eremin, I. M. Electronic correlations and superconducting instability in $La_3Ni_2O_7$ under high pressure. *Phys. Rev. B* **108**, L201121 (2023). URL https://doi.org/10.1103/PhysRevB.108.L201121.

[6] Luo, Z., Lv, B., Wang, M., Wú, W. & Yao, D.-X. High-T_c superconductivity in $La_3Ni_2O_7$ based on the bilayer two-orbital t-J model. *npj Quantum Mater.* **9**, 1–7 (2024). URL https://doi.org/10.1038/s41535-024-00668-w.

[7] Wú, W., Luo, Z., Yao, D.-X. & Wang, M. Superexchange and charge transfer in the nickelate superconductor $La_3Ni_2O_7$ under pressure. *Sci. China Phys. Mech. Astron.* **67**, 117402 (2024). URL https://doi.org/10.1007/s11433-023-2300-4.

[8] Wang, M., Wen, H.-H., Wu, T., Yao, D.-X. & Xiang, T. Normal and superconducting properties of $La_3Ni_2O_7$. *Chinese Physics Letters* **41**, 077402 (2024). URL https://dx.doi.org/10.1088/0256-307X/41/7/077402.

[9] Shilenko, D. A. & Leonov, I. V. Correlated electronic structure, orbital-selective behavior, and magnetic correlations in double-layer $La_3Ni_2O_7$ under pressure. *Phys. Rev. B* **108**, 125105 (2023). URL https://doi.org/10.1103/PhysRevB.108.125105.

[10] Yang, Y.-f., Zhang, G.-M. & Zhang, F.-C. Interlayer valence bonds and two-component theory for high-T_c superconductivity of $La_3Ni_2O_7$ under pressure. *Phys. Rev. B* **108**, L201108 (2023). URL https://doi.org/10.1103/PhysRevB.108.L201108.

[11] Huang, J., Wang, Z. D. & Zhou, T. Impurity and vortex states in the bilayer high-temperature superconductor $La_3Ni_2O_7$. *Phys. Rev. B* **108**, 174501 (2023). URL https://doi.org/10.1103/PhysRevB.108.174501.

[12] Christiansson, V., Petocchi, F. & Werner, P. Correlated electronic structure of $La_3Ni_2O_7$ under pressure. *Phys. Rev. Lett.* **131**, 206501 (2023). URL https://doi.org/10.1103/PhysRevLett.131.206501.

[13] Shen, Y., Qin, M. & Zhang, G.-M. Effective bi-

layer model hamiltonian and density-matrix renormalization group study for the high-tc superconductivity in $La_3Ni_2O_7$ under high pressure. *Chin. Phys. Lett.* **40**, 127401 (2023). URL https://doi.org/10.1088/0256-307X/40/12/127401.

[14] Gu, Y., Le, C., Yang, Z., Wu, X. & Hu, J. Effective model and pairing tendency in the bilayer ni-based superconductor $La_3Ni_2O_7$. *Phys. Rev. B* **111**, 174506 (2025). URL https://link.aps.org/doi/10.1103/PhysRevB.111.174506.

[15] Oh, H. & Zhang, Y.-H. Type-II $t-J$ model and shared superexchange coupling from hund's rule in superconducting $La_3Ni_2O_7$. *Phys. Rev. B* **108**, 174511 (2023). URL https://doi.org/10.1103/PhysRevB.108.174511.

[16] Liu, Y.-B., Mei, J.-W., Ye, F., Chen, W.-Q. & Yang, F. $s^{\pm}$-wave pairing and the destructive role of apical-oxygen deficiencies in $La_3Ni_2O_7$ under pressure. *Phys. Rev. Lett.* **131**, 236002 (2023). URL https://doi.org/10.1103/PhysRevLett.131.236002.

[17] Liao, Z. *et al.* Electron correlations and superconductivity in $La_3Ni_2O_7$ under pressure tuning. *Phys. Rev. B* **108**, 214522 (2023). URL https://doi.org/10.1103/PhysRevB.108.214522.

[18] Yang, Q.-G., Wang, D. & Wang, Q.-H. Possible $S_{\pm}$-wave superconductivity in $La_3Ni_2O_7$. *Phys. Rev. B* **108**, L140505 (2023). URL https://doi.org/10.1103/PhysRevB.108.L140505.

[19] Yang, J.-J., Yao, D.-X. & Wu, H.-Q. Correlation effects in a simplified bilayer two-orbital hubbard model at half filling. *Phys. Rev. B* **110**, 235155 (2024). URL https://doi.org/10.1103/PhysRevB.110.235155.

[20] Kaneko, T., Sakakibara, H., Ochi, M. & Kuroki, K. Pair correlations in the two-orbital hubbard ladder: Implications for superconductivity in the bilayer nickelate $La_3Ni_2O_7$. *Phys. Rev. B* **109**, 045154 (2024). URL https://doi.org/10.1103/PhysRevB.109.045154.

[21] Ouyang, Z., Gao, M. & Lu, Z.-Y. Absence of electron-phonon coupling superconductivity in the bilayer phase of $La_3Ni_2O_7$ under pressure. *npj Quantum Mater.* **9**, 1–6 (2024). URL https://doi.org/10.1038/s41535-024-00689-5.

[22] Heier, G., Park, K. & Savrasov, S. Y. Competing d_{xy} and $s_{\pm}$ pairing symmetries in superconducting $La_3Ni_2O_7$: LDA + FLEX calculations. *Phys. Rev. B* **109**, 104508 (2024). URL https://doi.org/10.1103/PhysRevB.109.104508.

[23] Zhang, Y., Lin, L.-F., Moreo, A., Maier, T. A. & Dagotto, E. Structural phase transition, s±-wave pairing, and magnetic stripe order in bilayered superconductor $La_3Ni_2O_7$ under pressure. *Nature Communications* **15**, 2470 (2024). URL https://doi.org/10.1038/s41467-024-46622-z.

[24] Zhang, Y., Lin, L.-F., Moreo, A., Maier, T. A. & Dagotto, E. Electronic structure, magnetic correlations, and superconducting pairing in the reduced Ruddlesden-Popper bilayer $La_3Ni_2O_6$ under pressure: Different role of $d_{3z^2-r^2}$ orbital compared with $La_3Ni_2O_7$. *Phys. Rev. B* **109**, 045151 (2024). URL https://doi.org/10.1103/PhysRevB.109.045151.

[25] Tian, Y.-H., Chen, Y., Wang, J.-M., He, R.-Q. & Lu, Z.-Y. Correlation effects and concomitant two-orbital $s_{\pm}$-wave superconductivity in $La_3Ni_2O_7$ under high pressure. *Phys. Rev. B* **109**, 165154 (2024). URL https://doi.org/10.1103/PhysRevB.109.165154.

[26] Ryee, S., Witt, N. & Wehling, T. O. Quenched pair breaking by interlayer correlations as a key to superconductivity in $La_3Ni_2O_7$. *Phys. Rev. Lett.* **133**, 096002 (2024). URL https://doi.org/10.1103/PhysRevLett.133.096002.

[27] Zhang, J.-X., Zhang, H.-K., You, Y.-Z. & Weng, Z.-Y. Strong pairing originated from an emergent Z_2 berry phase in $La_3Ni_2O_7$. *Phys. Rev. Lett.* **133**, 126501 (2024). URL https://doi.org/10.1103/PhysRevLett.133.126501.

[28] Ni, X.-S. *et al.* Spin density wave in the bilayered nickelate $La_3Ni_2O_{7-\delta}$ at ambient pressure. *npj Quantum Materials* **10**, 1–9 (2025). URL https://doi.org/10.1038/s41535-025-00740-z.

[29] Lu, C., Pan, Z., Yang, F. & Wu, C. Interlayer-coupling-driven high-temperature superconductivity in $La_3Ni_2O_7$ under pressure. *Phys. Rev. Lett.* **132**, 146002 (2024). URL https://doi.org/10.1103/PhysRevLett.132.146002.

[30] Qu, X.-Z. *et al.* Bilayer $t-J-J_{\perp}$ model and magnetically mediated pairing in the pressurized nickelate $La_3Ni_2O_7$. *Phys. Rev. Lett.* **132**, 036502 (2024). URL https://doi.org/10.1103/PhysRevLett.132.036502.

[31] Yang, H., Oh, H. & Zhang, Y.-H. Strong pairing from a small fermi surface beyond weak coupling: Application to $La_3Ni_2O_7$. *Phys. Rev. B* **110**, 104517 (2024). URL https://doi.org/10.1103/PhysRevB.110.104517.

[32] Fan, Z. *et al.* Superconductivity in nickelate and cuprate superconductors with strong bilayer coupling. *Phys. Rev. B* **110**, 024514 (2024). URL https://doi.org/10.1103/PhysRevB.110.024514.

[33] Sakakibara, H., Kitamine, N., Ochi, M. & Kuroki, K. Possible high T_c superconductivity in $La_3Ni_2O_7$ under high pressure through manifestation of a nearly half-filled bilayer hubbard model. *Phys. Rev. Lett.* **132**, 106002 (2024). URL https://doi.org/10.1103/PhysRevLett.132.106002.

[34] Cao, Y. & Yang, Y.-f. Flat bands promoted by hund's rule coupling in the candidate double-layer high-temperature superconductor $La_3Ni_2O_7$ under high pressure. *Phys. Rev. B* **109**, L081105 (2024). URL https://doi.org/10.1103/PhysRevB.109.L081105.

[35] Jiang, R., Hou, J., Fan, Z., Lang, Z.-J. & Ku, W. Pressure driven fractionalization of ionic spins results in cupratelike high-T_c superconductivity in $La_3Ni_2O_7$. *Phys. Rev. Lett.* **132**, 126503 (2024). URL https://doi.org/10.1103/PhysRevLett.132.126503.

[36] Chen, X., Jiang, P., Li, J., Zhong, Z. & Lu, Y. Charge and spin instabilities in superconducting $La_3Ni_2O_7$. *Phys. Rev. B* **111**, 014515 (2025). URL https://doi.org/10.1103/PhysRevB.111.014515.

[37] Yang, J. *et al.* Orbital-dependent electron correlation in double-layer nickelate $La_3Ni_2O_7$. *Nat Commun* **15**, 4373 (2024). URL https://doi.org/10.1038/s41467-024-48701-7.

[38] Zhang, Y. *et al.* High-temperature superconductivity with zero resistance and strange-metal behaviour in $La_3Ni_2O_{7-\delta}$. *Nat. Phys.* **20**, 1269–1273 (2024). URL https://doi.org/10.1038/s41567-024-02515-y.

[39] Hou, J. *et al.* Emergence of high-temperature superconducting phase in pressurized $La_3Ni_2O_7$ crystals. *Chin. Phys. Lett.* **40**, 117302 (2023). URL https://dx.doi.org/10.1088/0256-307X/40/11/117302.

[40] Fan, S. *et al.* Tunneling spectra with gaplike features ob-

served in nickelate $La_3Ni_2O_7$ at ambient pressure. *Phys. Rev. B* **110**, 134520 (2024). URL https://doi.org/10.1103/PhysRevB.110.134520.

[41] Wang, G. *et al.* Pressure-Induced Superconductivity In Polycrystalline $La_3Ni_2O_{7-\delta}$. *Phys. Rev. X* **14**, 011040 (2024). URL https://doi.org/10.1103/PhysRevX.14.011040.

[42] Liu, Z. *et al.* Electronic correlations and partial gap in the bilayer nickelate $La_3Ni_2O_7$. *Nat Commun* **15**, 7570 (2024). URL https://doi.org/10.1038/s41467-024-52001-5.

[43] Zhang, M. *et al.* $s^{\pm}$-wave superconductivity in pressurized $La_4Ni_3O_{10}$. *Phys. Rev. B* **110**, L180501 (2024). URL https://doi.org/10.1103/PhysRevB.110.L180501.

[44] Jiang, K.-Y., Cao, Y.-H., Yang, Q.-G., Lu, H.-Y. & Wang, Q.-H. Theory of pressure dependence of superconductivity in bilayer nickelate $La_3Ni_2O_7$. *Phys. Rev. Lett.* **134**, 076001 (2025). URL https://link.aps.org/doi/10.1103/PhysRevLett.134.076001.

[45] Shao, Z.-Y., Ji, J.-H., Wu, C., Yao, D.-X. & Yang, F. Possible high-temperature superconductivity driven by perpendicular electric field in the $La_3Ni_2O_7$ single-bilayer film at ambient pressure (2024). URL https://arxiv.org/abs/2411.13554. 2411.13554.

[46] Zhu, Y. *et al.* Superconductivity in pressurized trilayer $La_4Ni_3O_{10-\delta}$ single crystals. *Nature* **631**, 531–536 (2024). URL https://doi.org/10.1038/s41586-024-07553-3.

[47] Zhang, M. *et al.* Superconductivity in trilayer nickelate $La_4Ni_3O_{10}$ under pressure. *Physical Review X* **15**, 021005 (2025). URL https://doi.org/10.1103/PhysRevX.15.021005.

[48] Ko, E. K. *et al.* Signatures of ambient pressure superconductivity in thin film $La_3Ni_2O_7$. *Nature* **638**, 935–940 (2025). URL https://doi.org/10.1038/s41586-024-08525-3.

[49] Zhou, G. *et al.* Ambient-pressure superconductivity onset above 40 K in $(La,Pr)_3Ni_2O_7$ films. *Nature* **640**, 641–646 (2025). URL https://doi.org/10.1038/s41586-025-08755-z.

[50] Chen, C.-Q., Luo, Z., Wang, M., Wú, W. & Yao, D.-X. Trilayer multiorbital models of $La_4Ni_3O_{10}$. *Phys. Rev. B* **110**, 014503 (2024). URL https://link.aps.org/doi/10.1103/PhysRevB.110.014503.

[51] Xu, S. *et al.* Origin of the density wave instability in trilayer nickelate $La_4Ni_3O_{10}$ revealed by optical and ultrafast spectroscopy. *Phys. Rev. B* **111**, 075140 (2025). URL https://link.aps.org/doi/10.1103/PhysRevB.111.075140.

[52] Sakakibara, H. *et al.* Theoretical analysis on the possibility of superconductivity in the trilayer Ruddlesden-Popper nickelate $La_4Ni_3O_{10}$ under pressure and its experimental examination: Comparison with $La_3Ni_2O_7$. *Phys. Rev. B* **109**, 144511 (2024). URL https://link.aps.org/doi/10.1103/PhysRevB.109.144511.

[53] Li, Q. *et al.* Signature of Superconductivity in Pressurized $La_4Ni_3O_{10}$. *Chin. Phys. Lett.* **41**, 017401 (2024). URL https://doi.org/10.1088/0256-307X/41/1/017401.

[54] Hu, X., Qiu, W., Chen, C.-Q., Luo, Z. & Yao, D.-X. Electronic structures and multi-orbital models of $La_3Ni_2O_7$ thin films at ambient pressure (2025). URL https://arxiv.org/abs/2503.17223. 2503.17223.

[55] Li, J. *et al.* Structural transition, electric transport, and electronic structures in the compressed trilayer nickelate $La_4Ni_3O_{10}$. *Science China Physics, Mechanics & Astronomy* **67**, 117403 (2024). URL https://doi.org/10.1007/s11433-023-2329-x.

[56] Wang, Y., Jiang, K., Wang, Z., Zhang, F.-C. & Hu, J. Electronic and magnetic structures of bilayer $La_3Ni_2O_7$ at ambient pressure. *Physical Review B* **110**, 205122 (2024). URL https://doi.org/10.1103/PhysRevB.110.205122.

[57] Geisler, B., Hamlin, J. J., Stewart, G. R., Hennig, R. G. & Hirschfeld, P. J. Structural transitions, octahedral rotations, and electronic properties of $A_3Ni_2O_7$ rare-earth nickelates under high pressure. *npj Quantum Materials* **9**, 38 (2024). URL https://doi.org/10.1038/s41535-024-00648-0.

[58] Li, J. *et al.* Identification of superconductivity in bilayer nickelate $La_3Ni_2O_7$ under high pressure up to 100 GPa. *National Science Review* nwaf220 (2025). URL https://doi.org/10.1093/nsr/nwaf220.

[59] Zhang, Y., Lin, L.-F., Moreo, A., Maier, T. A. & Dagotto, E. Magnetic correlations and pairing tendencies of the hybrid stacking nickelate superlattice $La_7Ni_5O_{17}$ ($La_3Ni_2O_7/La_4Ni_3O_{10}$) under pressure (2024). URL https://arxiv.org/abs/2408.07690. 2408.07690.

[60] Chen, X. *et al.* Polymorphism in the Ruddlesden–Popper nickelate $La_3Ni_2O_7$: Discovery of a hidden phase with distinctive layer stacking. *Journal of the American Chemical Society* **146**, 3640–3645 (2024). URL https://doi.org/10.1021/jacs.3c14052.

[61] Puphal, P. *et al.* Unconventional crystal structure of the high-pressure superconductor $La_3Ni_2O_7$. *Phys. Rev. Lett.* **133**, 146002 (2024). URL https://doi.org/10.1103/PhysRevLett.133.146002.

[62] Li, F. *et al.* Design and synthesis of three-dimensional hybrid Ruddlesden-Popper nickelate single crystals. *Phys. Rev. Mater.* **8**, 053401 (2024). URL https://link.aps.org/doi/10.1103/PhysRevMaterials.8.053401.

[63] Ouyang, Z., He, R.-Q. & Lu, Z.-Y. Phase diagrams and two key factors to superconductivity of Ruddlesden-Popper nickelates. *Phys. Rev. B* **112**, 045127 (2025). URL https://link.aps.org/doi/10.1103/1412-nfzm.

[64] Shi, M. *et al.* Pressure induced superconductivity in hybrid Ruddlesden–Popper La5Ni3O11 single crystals. *Nature Physics* **21**, 1780–1786 (2025). URL https://doi.org/10.1038/s41567-025-03023-3.

[65] Zhang, Y. *et al.* Electronic structure, magnetic and pairing tendencies of alternating single-layer bilayer stacking nickelate $La_5Ni_3O_{11}$ under pressure (2025). URL https://arxiv.org/abs/2503.05075. 2503.05075.

[66] LaBollita, H. & Botana, A. S. Correlated electronic structure of the alternating single-layer bilayer nickelate $La_5Ni_3O_{11}$ (2025). URL https://arxiv.org/abs/2505.07394. 2505.07394.

[67] Yao, D. X. & Carlson, E. W. Spin-wave dispersion in half-doped $La_{3/2}Sr_{1/2}NiO_4$. *Phys. Rev. B* **75**, 012414 (2007). URL https://link.aps.org/doi/10.1103/PhysRevB.75.012414.

[68] Freeman, P. G. *et al.* Inward dispersion of the spin excitation spectrum of stripe-ordered $La_2NiO_{4+\delta}$. *Phys. Rev. B* **80**, 144523 (2009). URL https://link.aps.org/doi/10.1103/PhysRevB.80.144523.

[69] See Supplementary Information for phonon spectrum and the comparison of band structures at AP and HP.

[70] Takimoto, T., Hotta, T. & Ueda, K. Strong-coupling

theory of superconductivity in a degenerate hubbard model. *Phys. Rev. B* **69**, 104504 (2004). URL https://doi.org/10.1103/PhysRevB.69.104504.

[71] Yada, K. & Kontani, H. Origin of weak pseudogap behaviors in $Na_{0.35}CoO_2$: Absence of small hole pockets. *J. Phys. Soc. Jpn.* **74**, 2161–2164 (2005). URL https://doi.org/10.1143/JPSJ.74.2161.

[72] Kubo, K. Pairing symmetry in a two-orbital hubbard model on a square lattice. *Phys. Rev. B* **75**, 224509 (2007). URL https://doi.org/10.1103/PhysRevB.75.224509.

[73] Graser, S., Maier, T., Hirschfeld, P. & Scalapino, D. Near-degeneracy of several pairing channels in multiorbital models for the Fe pnictides. *New J. Phys.* **11**, 025016 (2009). URL https://iopscience.iop.org/article/10.1088/1367-2630/11/2/025016.

[74] Liu, F., Liu, C.-C., Wu, K., Yang, F. & Yao, Y. $d+id'$ chiral superconductivity in bilayer silicene. *Phys. Rev. Lett.* **111**, 066804 (2013). URL https://doi.org/10.1103/PhysRevLett.111.066804.

[75] Zhang, M., Hao, J.-J., Wu, X. & Yang, F. Lifshitz transition enhanced triplet pz-wave superconductivity in hydrogen-doped KCr_3As_3. *Phys. Rev. B* **105**, 134509 (2022). URL https://doi.org/10.1103/PhysRevB.105.134509.

[76] Kuroki, K., Onari, S., Arita, R. *et al.* Unconventional pairing originating from the disconnected fermi surfaces of superconducting $LaFeAsO_{1-x}F_x$. *Phys. Rev. Lett.* **101**, 087004 (2008). URL https://doi.org/10.1103/PhysRevLett.101.087004.

[77] Kopeć, T. K. & Polak, T. P. Superconducting phase transition in quantum three-dimensional josephson junction arrays: c-axis anisotropy and charge frustration effects. *Phys. Rev. B* **62**, 14419–14426 (2000). URL https://link.aps.org/doi/10.1103/PhysRevB.62.14419.

[78] Kresse, G. & Furthmuller, J. Efficiency of ab-initio total energy calculations for metals and semiconductors using a plane-wave basis set. *Computational Materials Science* **6**, 15–50 (1996). URL https://doi.org/10.1016/0927-0256(96)00008-0.

[79] Kresse, G. & Furthmuller, J. Efficient iterative schemes for ab initio total-energy calculations using a plane-wave basis set. *Physical Review B* **54**, 11169–11186 (1996). URL https://link.aps.org/doi/10.1103/PhysRevB.54.11169.

[80] Blochl, P. E. Projector augmented-wave method. *Physical Review B* **50**, 17953–17979 (1994). URL https://link.aps.org/doi/10.1103/PhysRevB.50.17953.

[81] Kresse, G. & Joubert, D. From ultrasoft pseudopotentials to the projector augmented-wave method. *Physical Review B* **59**, 1758–1775 (1999). URL https://link.aps.org/doi/10.1103/PhysRevB.59.1758.

[82] Perdew, J. P., Burke, K. & Ernzerhof, M. Generalized gradient approximation made simple. *Phys. Rev. Lett.* **77**, 3865–3868 (1996). URL https://link.aps.org/doi/10.1103/PhysRevLett.77.3865.

[83] Dudarev, S. L., Botton, G. A., Savrasov, S. Y., Humphreys, C. J. & Sutton, A. P. Electron-energy-loss spectra and the structural stability of nickel oxide: An LSDA+U study. *Phys. Rev. B* **57**, 1505–1509 (1998). URL https://link.aps.org/doi/10.1103/PhysRevB.57.1505.

[84] Mostofi, A. A. *et al.* wannier90: A tool for obtaining maximally-localised wannier functions. *Computer Physics Communications* **178**, 685–699 (2008). URL https://doi.org/10.1016/j.cpc.2007.11.016.

[85] Wu, X., Yuan, J., Liang, Y., Fan, H. & Hu, J. g-wave pairing in bis2 superconductors. *Europhysics Letters* **108**, 27006 (2014). URL https://dx.doi.org/10.1209/0295-5075/108/27006.

[86] Ma, T., Yang, F., Yao, H. & Lin, H.-Q. Possible triplet $p+ip$ superconductivity in graphene at low filling. *Phys. Rev. B* **90**, 245114 (2014). URL https://link.aps.org/doi/10.1103/PhysRevB.90.245114.

Acknowledgements

We are grateful for the discussion with Chen Lu. This work is supported by National Natural Science Foundation of China (Grants No. 12494591, No. 92165204, No. 12234016, No. 12074031), National Key Research and Development Program of China (2022YFA1402802), Guangdong Provincial Key Laboratory of Magnetoelectric Physics and Devices (2022B1212010008), Guangdong Fundamental Research Center for Magnetoelectric Physics (2024B0303390001), and Guangdong Provincial Quantum Science Strategic Initiative (GDZX2401010). Ming Zhang is supported by the Zhejiang Provincial Natural Science Foundation of China under Grant No. ZCLQN25A0402.

Author contribution

Dao-Xin Yao and Fan Yang conceived and designed the project. Ming Zhang and Cui-Qun Chen performed the numerical calculations for DFT, TB model, and RPA calculations. All authors contributed to the discussion of the results and wrote the paper.

Competing interests

The authors declare no competing interests.

Addition information

Supplementary information The online version contains supplementary information available at